

ISAC 4D Imaging System Based on 5G Downlink Millimeter Wave Signal

Bohao Lu¹, Zhiqing Wei^{1,*}, Lin Wang¹, Ruiyun Zhang¹, Zhiyong Feng¹
¹Beijing University of Posts and Telecommunications, Beijing 100876, China
¹Email: {bohaolu, weizhiqing, wlwl, zhangruiyun, fengzy}@bupt.edu.cn

Abstract—Integrated Sensing and Communication (ISAC) has become a key technology for the 5th generation (5G) and 6th generation (6G) wireless communications due to its high spectrum utilization efficiency. Utilizing infrastructure such as 5G Base Stations (BS) to realize environmental imaging and reconstruction is important for promoting the construction of smart cities. Current 4D imaging methods utilizing Frequency Modulated Continuous Wave (FMCW) based Fast Fourier Transform (FFT) are not suitable for ISAC scenarios due to the higher bandwidth occupation and lower resolution. We propose a 4D (3D-Coordinates, Velocity) imaging method with higher sensing accuracy based on 2D-FFT with 2D-MUSIC utilizing standard 5G Downlink (DL) millimeter wave (mmWave) signals. To improve the sensing precision we also design a transceiver antenna array element arrangement scheme based on MIMO virtual aperture technique. We further propose a target detection algorithm based on multi-dimensional Constant False Alarm (CFAR) detection, which optimizes the ISAC imaging signal processing flow and reduces the computational pressure of signal processing. Simulation results show that our proposed method has better imaging results. The code is publicly available at https://github.com/MrHaobolu/ISAC_4D_Imaging.git.

Index Terms—ISAC, 2D-FFT with 2D-MUSIC, 5G mmWave, MIMO, virtual aperture, CFAR

I. INTRODUCTION

A. Background and Motivation

The development of 5G and 6G wireless communications toward higher frequency bands and larger bandwidths has significantly improved the sensing ability of communication signals. ISAC-based technology using widely available wireless communication signals to achieve imaging and 4D reconstruction of urban environment is important for digital twin and smart city construction [1]. Compared with traditional imaging with additional optical detection equipment, ISAC-based wireless imaging has low-deployment-cost, privacy protection, and robustness in severe weather.

B. Related Works

The majority of current work in wireless imaging focuses on 3D or 4D imaging using Frequency Modulated Continuous Wave (FMCW) radar, which primarily uses FFT-based algorithms for echo signal processing [2]. Jiang et al. [3] proposed a wireless imaging method that embeds dual pulse repetition frequency (dual-PRF) waveforms into a time-division

multiplexing & Doppler-division multiplexing MIMO (TDM-DDM-MIMO) framework and a super-resolution Direction of Arrival (DoA) estimation Depth Convolutional Network: CV-DCN to obtain high-resolution 4D point cloud images. Santra et al. [4] proposed a MIMO radar imaging scheme based on roughly orthogonal FMCW waveforms. Sun et al. [5] proposed a high-resolution imaging radar system using the virtual 2D sparse array. The above FFT-base 4D imaging algorithms have limited resolution compared to Multiple Signal Classification (MUSIC)-based algorithms. Besides, the FMCW is not suitable for ISAC because of its poor communication capability.

Orthogonal frequency division multiplexing (OFDM)-based ISAC waveform is widely studied [6], but there are few related works on OFDM radar-based 4D imaging algorithms. Guan et al. [7] built a high-resolution 3D radar imaging system using 5G millimeter wave (mmWave) signals. There is a lack of estimation of targets' velocities and the use of FFT-based signal processing algorithms leads to a significantly limited 3D point cloud resolution among the above work.

In order to improve the resolution of DoA estimation and reduce the false alarm probability of 4D point cloud detection, the virtual aperture technique [8] with Constant False Alarm Rate (CFAR) [9] detection has been introduced in related research. However, the virtual aperture transceiver antenna design for DL active sensing of 5G NR BS is not well designed, and the current widely used CFAR detection algorithms cannot overcome the small target missing detection problem caused by strong interference. Therefore, the improvement of transceiver antenna design and CFAR detection algorithm is also a key issue to achieve 4D imaging in ISAC scenarios.

C. Contributions

To solve the above problems, we propose an OFDM DL ISAC imaging algorithm based on FFT and MUSIC using 5G mmWave signals. The main contributions and innovations of this paper are summarized as follows.

- We propose a BS-side active 4D imaging sensing algorithm using standard 5G NR mmWave signal containing Comb4 structured Positioning Reference Signal (PRS). The proposed algorithm can simultaneously estimate the range, velocity, and azimuth & pitch angle information (4D information) for a large number of scatter points.
- We propose a transceiver antenna array design based on virtual aperture technology, which can effectively improve the resolution of DoA estimation by increasing the virtual

This work was supported in part by the National Key Research and Development Program under Grant 2020YFA0711302, in part by the National Natural Science Foundation of China (NSFC) under Grant 62271081, 92267202, and U21B2014.

array when the size of transceiver antenna array in the current BS is limited.

- We propose a two-stage scattering point detection algorithm based on CFAR detection. The proposed algorithm uses OSCA (Ordered Statistics & Cell Averaging)-CFAR detection algorithm for the Range-Doppler Map (RDM) obtained by 2D-FFT and CA-CFAR detection algorithm for 2D-MUSIC DoA estimation results, which can reduce the computational complexity and reduce the probability of false alarm compared to the single constant threshold detection method.

II. SYSTEM AND SIGNAL MODELS

A. DL ISAC Imaging Model

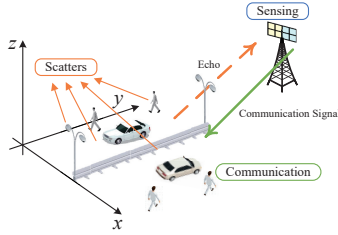


Fig. 1. DL ISAC Imaging Scenario.

As shown in Fig. 1, we consider the DL ISAC imaging scenario between the 5G BS, the User Equipment (UE), and the user's environment. The scatterers in the environment include vehicles, pedestrians, road infrastructure, etc. The 5G BS is equipped with two spatially well-separated Uniform Planar Arrays (UPAs). At the BS side, one UPA is used to transmit DL ISAC signals and the other UPA is used to continuously receive the echoes of ISAC signals for estimating the range, velocity, and DoAs of the ambient scatterers for 4D imaging. At the UE side, the UE receives the ISAC signals to demodulate the communication data. The transmit and receive arrays of the BS have dimensions $P_t \times Q_t$ and $P_r \times Q_r$, whose array element spacing and the arrangement will be described in detail below.

B. UPAs Model and Virtual Aperture

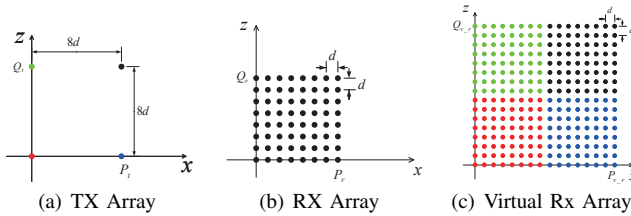


Fig. 2. MIMO array design with the transmitting array in (a), the receiving array in (b) and the corresponding Virtual Rx (VRx) array in (c).

In order to simultaneously measure the pitch and azimuth angles of DoA and obtain higher angular resolution, we design transmit-receive UPAs as shown in Fig. 2. The receiving antenna array element spacing is half wavelength, i.e., $d = \lambda/2$, where λ represents the signal wavelength, the transmit UPA is a 2×2 array with a spacing of $8d$, the receive UPA is an 8×8

array with a spacing of d , and the corresponding receive UPA is a 16×16 array with a spacing of d .

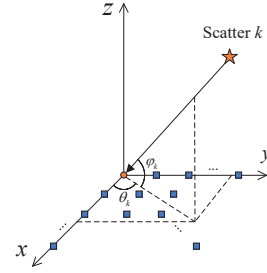


Fig. 3. Schematic diagrams of the geometric relationship between the target and the UPAs.

The geometric relationship between the k th scattering point and BS is shown in Fig. 3, with the azimuth and pitch angles noted as (θ_k, φ_k) . The antenna array element in the virtual receiving array is denoted as $A_{v_r}(p_{v_r}, q_{v_r})$, and the reference antenna array element is $A_{v_r}(1, 1)$, then the phase difference between $A_{v_r}(p_{v_r}, q_{v_r})$ and $A_{v_r}(1, 1)$ caused by the k th scattering point can be expressed by (1).

$$\begin{aligned} & \Delta\phi_{v_r}(p_{v_r}, q_{v_r})_{(\theta_k, \varphi_k)} \\ &= e^{-\xi j 2\pi \frac{d[(p_{v_r}-1)\cos\theta_k + \psi(q_{v_r}-1)\sin\theta_k]\cos\varphi_k}{\lambda}} \\ & \begin{cases} \xi = 1, \psi = 1, \theta_k < 90^\circ, \varphi_k < 90^\circ \\ \xi = -1, \psi = -1, \theta_k > 90^\circ, \varphi_k < 90^\circ \\ \xi = 1, \psi = -1, \theta_k < 90^\circ, \varphi_k > 90^\circ \\ \xi = -1, \psi = 1, \theta_k > 90^\circ, \varphi_k > 90^\circ \end{cases} \end{aligned} \quad (1)$$

As shown in (2), the VRx array phase difference matrix \mathbf{A}_k corresponding to the k th target is obtained from (1).

$$\mathbf{A}_k(p_{v_r}, q_{v_r}) = \Delta\phi_{v_r}(p_{v_r}, q_{v_r})_{(\theta_k, \varphi_k)} \quad (2)$$

C. DL ISAC Signal Model

As shown in Fig. 4 (a) we use the structure of Comb4 with 4 symbols and the PRS mapped OFDM signal model is shown in Fig. 4 (b) [10]. In a time slot, PRS occupies N_{PRS_t} OFDM symbols for the time domain where PRS_t is the set of symbols carrying PRS, and PRS occupies N_{PRS_f} subcarriers at certain spacings for the frequency domain where PRS_f is the set of subcarriers carrying PRS.

The continuous time domain OFDM signal can be described as

$$y(t) = \sum_{m=0}^{N_{sym}-1} \sum_{n=0}^{N_c-1} s_{Tx}(n, m) e^{j2\pi f_n t} \text{rect}\left(\frac{t - mT_{OFDM}}{T_{OFDM}}\right) \quad (3)$$

where $s_{Tx}(n, m)$ represents the modulated OFDM symbol in the n th subcarrier of m th OFDM symbol, N_{sym} is the number of OFDM symbols and N_c is the number of subcarriers. T_{OFDM} is the total duration of the OFDM symbol which satisfies $T_{OFDM} = T + T_{CP}$, where T is the effective OFDM symbol duration and T_{CP} is the cyclic prefix duration. $\Delta f = 1/T$ is the frequency interval of subcarriers, f_n is the frequency

of the n th subcarriers that carrying the modulation symbol, $\text{rect}\left(\frac{t}{T_{\text{OFDM}}}\right)$ is the rectangular function which is equal to 1 for $0 \leq t \leq T_{\text{OFDM}}$ and 0 for otherwise.

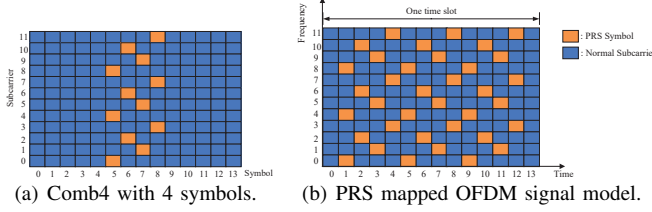


Fig. 4. PRS time-frequency structure schematic.

When $n \in \text{PRS}_f, m \in \text{PRS}_t$, $s(n, m)$ takes the GOLD sequence value, otherwise $s(n, m)$ carries random communication information. The PRS occupies the 2nd-13th OFDM symbols in a time slot, and we insert a set of PRS every 4th-time slot. The frequency of the subcarriers carrying PRS symbols f_n satisfies (4) when $m \in \text{PRS}_t$, where $K_{\text{Comb}}^{\text{PRS}}$ is the comb size of PRS, n_0 is the index of the first subcarrier carrying PRS.

$$f_n = (n \times K_{\text{Comb}}^{\text{PRS}} + n_0) \Delta f, n = 0, \dots, N_{\text{PRS}_f} - 1 \quad (4)$$

The designed DL ISAC imaging signal satisfies $K_{\text{Comb}}^{\text{PRS}}$ and $n_0 \in [0, 2, 1, 3]$ in turn. The relation between n_0 and m is shown in (5), where mod refers to a modulo operation.

$$n_0 = \frac{m \bmod K_{\text{Comb}}^{\text{PRS}}}{2} + \frac{3}{4} \left[1 - (-1)^{m \bmod K_{\text{Comb}}^{\text{PRS}}} \right] \quad (5)$$

D. ISAC Received Signal Model

The received signal can be described as (6) when the OFDM signal shown in (3) is reflected by the k th scatterer. R_k and $f_d(k)$ is the range and doppler shift of k th scatterer, respectively. G_k represents the attenuation factor associated with the path loss, radar cross section (RCS) of the k th scatterer.

$$y_{n,m,k}^{Rx}(t) = G_k \sum_{m=0}^{N_{\text{sym}}-1} e^{j2\pi f_d(k)t} \sum_{n=0}^{N_c-1} s_{Rx}(n, m, k) \times e^{j2\pi f_n \left(t - \frac{2R_k}{c}\right)} \times \text{rect}\left(\frac{t - mT_{\text{OFDM}} - \frac{2R_k}{c}}{T_{\text{OFDM}}}\right) \quad (6)$$

The relationship between the received modulation symbols $s_{Rx}(n, m, k)$ and the transmitted modulation symbol $s_{Tx}(n, m)$ can be described by (7) from (3).

$$s_{Rx}(n, m, k) = G_k s_{Tx}(n, m) e^{-j2\pi f_n \frac{2R_k}{c}} e^{j2\pi f_d(k) m T_{\text{OFDM}}} \quad (7)$$

Dividing the received modulation symbols $s_{Rx}(n, m, k)$ and the transmitted modulation symbol $s_{Tx}(n, m)$, the following matrix $s_g(n, m, k)$ is obtained.

$$s_g(n, m, k) = \frac{s_{Rx}(n, m, k)}{s_{Tx}(n, m)} = G_k \left(\vec{k}_r \otimes \vec{k}_d \right) \quad (8)$$

where $\vec{k}_r = \left(0, e^{-j2\pi \Delta f \frac{2R_k}{c}}, \dots, e^{-j2\pi(N_c-1)\Delta f \frac{2R_k}{c}}\right)$ and $\vec{k}_d = \left(0, e^{j2\pi T_{\text{OFDM}} f_d(k)}, \dots, e^{j2\pi(N_{\text{sym}}-1)T_{\text{OFDM}} f_d(k)}\right)$ are the

two vectors carrying the range and the doppler information. \otimes refers to a dyadic product [11].

The detection information matrix \mathbf{A}_S of all array elements in the corresponding virtual receiving antenna array can be obtained by combining (2) and (8) as shown in (9).

$$\mathbf{A}_S = \sum_k s_g(n, m, k) \mathbf{A}_k \quad (9)$$

The \mathbf{A}_S in our simulation work exists in the form of 4D arrays which contain the dimensions of fast time dimension, slow time dimension, horizontal antenna array dimension and vertical antenna array dimension. In actual ISAC 4D imaging system, \mathbf{A}_S represents the environmental scatterer reflection signal received by UPA.

III. METHODOLOGY OF SIGNAL PROCESSING

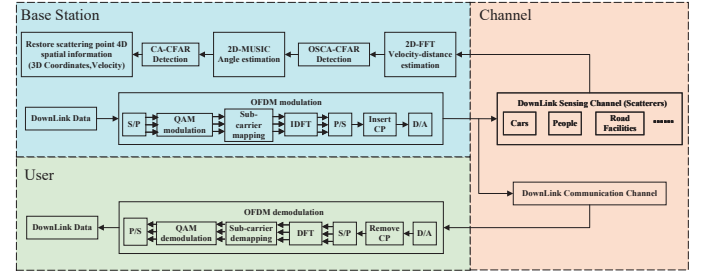


Fig. 5. Diagram of the DL ISAC signal processing.

In this section, we demonstrate the sensing and communication processing method as shown in Fig. 5. We present the simulation method of ISAC imaging environment, the ISAC imaging sensing processing method, and the ISAC Imaging communication processing method.

A. ISAC Imaging Environment Simulation

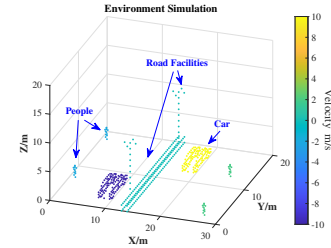


Fig. 6. Simulation of environmental scattering points.

As shown in Fig. 6, we used scatter points to depict the contours of people, vehicles and road infrastructure in the simulated environment. We also added $\pm 2\text{m/s}$, $\pm 10\text{m/s}$ and stationary velocity information for the above three types of targets respectively. In addition, we assumed that the ISAC BS is suspended at $P_{BS}(x, y, z) = (14, 100, 20)$.

B. ISAC Sensing Signal Processing

In this section we first introduce the range and Doppler detection based on 2D-FFT and OSCA-CFAR algorithms, then introduce the DoAs estimation based on 2D-MUSIC and CA-CFAR algorithms.

1) *ISAC Imaging Range and Doppler Detection*: The \vec{k}_r in (8) is the linear phase shift vector along the fast time axis caused by range R . Therefore, the scatters' range can be estimated by using (8) to initially process the received signal of each antenna array element and then performing the Inverse Discrete Fourier Transform (IDFT) along the subcarrier dimension.

$$\begin{aligned} R(\alpha) &= \text{IDFT}[k_r(n)] = \frac{1}{N_c} \sum_{n=0}^{N_c-1} k_r(n) e^{jn\alpha \frac{2\pi}{N_c}} \\ &= \frac{1}{N_c} \sum_{n=0}^{N_c-1} e^{-j2\pi n \Delta f \frac{2R}{c}} e^{jn\alpha \frac{2\pi}{N_c}}, \alpha = 0, \dots, N_c - 1 \end{aligned} \quad (10)$$

where $R(\alpha)$ obtains peak value when $\alpha = \left\lfloor \frac{2R\Delta f N_c}{c} \right\rfloor$. The \vec{k}_d in (8) is the linear phase shift vector along the slow time axis caused by velocity v_k . Similarly v_k can be estimated by performing a Discrete Fourier Transform (DFT) along the OFDM symbol dimension.

$$\begin{aligned} v(\beta) &= \text{DFT}[k_d(m)] = \sum_{m=0}^{N_{\text{sym}}-1} k_d(m) e^{-jm\beta \frac{2\pi}{N_{\text{sym}}}} \\ &= \sum_{m=0}^{N_{\text{sym}}-1} e^{j2\pi m T_{\text{OFDM}} \frac{2v_k f_c}{c}} e^{-jm\beta \frac{2\pi}{N_{\text{sym}}}}, \beta = 0, \dots, N_{\text{sym}} - 1 \end{aligned} \quad (11)$$

where $v(\beta)$ obtains peak value when β in (11) satisfies $\beta = \left\lfloor \frac{2v_k f_c T_{\text{OFDM}} N_{\text{sym}}}{c} \right\rfloor$.

We denote the 2D-FFT processing result of s_g in (8) as $s_g^{R,v}$ which is known as RDM, and then we estimate the range and velocity of scattering points using 2D OSCA-CFAR detection in $s_g^{R,v}$. As shown in Fig. 7 (a) we select a reference window of size 9×9 within the RDM.

- Firstly, the 1D OS-CFAR is applied to the sliding reference window by column and the γ th value of each column is selected as the noise estimate of this sliding window. We take $\gamma = \lfloor 0.75N \rfloor$, where N is the number of reference cells.
- Then the noise estimation values of the above columns are averaged by row as shown in (12) as the noise threshold of the Center Detection Unit (CUT) in reference window.

$$\bar{\mu}(\gamma) = \frac{1}{N} \sum_{n=1}^N X_{(\gamma),n} \quad (12)$$

where $X_{(\gamma),n}$ represents the noise reference value selected by OS-CFAR, $N = 9$.

- As shown in (13), the detection threshold factor T_f of this CUT is only related to the number of reference units N with the specified false alarm probability P_{fa} . Finally, the detection threshold $T = T_f \times \bar{\mu}(\gamma)$ for a single CUT can be obtained, and the 2D adaptive detection threshold can be obtained by applying the above operations to all CUTs in the RDM as shown in Fig. 7 (d)-(e).

$$T_f = (P_{fa})^{-\frac{1}{N}} - 1 \quad (13)$$

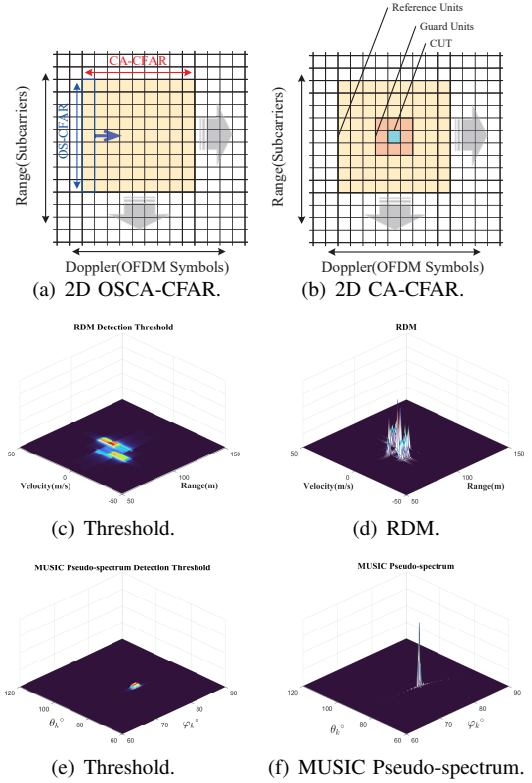


Fig. 7. (a)-(b) are the sliding reference window design for OSCA-CFAR and CA-CFAR, (c)-(d) are the RDM and its detection threshold and (e)-(f) are the MUSIC Pseudo-spectrum and its detection threshold.

2) *ISAC Imaging DoAs Estimation*: The peak of the RDM indicates the presence of targets with velocity v and range R but 2D angles are unknown. As shown in (14), we combine the RDM peaks detected by OSCA-CFAR of all receiving antenna elements into k_m ($k_m < k$) manifolds for MUSIC-based DoA estimation.

$$\mathbf{A}_{k_m}(p_{v-r}, q_{v-r}) = \sum_t \mathbf{G}_t \mathbf{A}_t = \sum_t \mathbf{G}_t \Delta \phi_{v-r}(p_{v-r}, q_{v-r})_{(\theta_t, \varphi_t)} \quad (14)$$

We take $(\mathbf{A}_{k_m})_{1,:}$ (row where the reference element is located) and $(\mathbf{A}_{k_m})_{:,1}$ (column where the reference element is located) of \mathbf{A}_{k_m} to construct the searching manifolds, which are related to the 2D angle $\mathbf{p} = (\theta, \varphi)$ of the targets simultaneously, and eventually just multiply the two search results to get the 2D angle information of t targets in \mathbf{A}_{k_m} . Take $(\mathbf{A}_{k_m})_{:,1}$ as an example to introduce the angle search process.

Since the strong correlation of the received signals, it is necessary to use the MUSIC algorithm based on spatial smoothing. As shown in Fig. 8, we can define the forward spatial smoothing matrix $\mathbf{R}_f = \frac{1}{L} \sum_{l=1}^L \mathbf{R}_l^f$, and similarly the backward

spatial smoothing matrix $\mathbf{R}_b = \frac{1}{L} \sum_{l=1}^L \mathbf{R}_l^b$, where \mathbf{R}_l^f and \mathbf{R}_l^b are the covariance matrices of the subarray and L is the number of subarray elements. Then use the average of them $\mathbf{R}_X = \frac{\mathbf{R}_f + \mathbf{R}_b}{2}$ to replace the original covariance matrix.

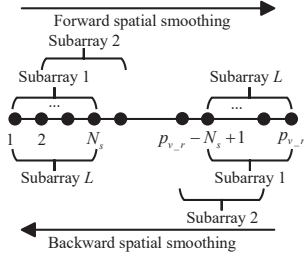


Fig. 8. Schematic of the forward and backward space smoothing algorithm.

We can get (15) by applying eigenvalue decomposition to \mathbf{R}_X .

$$[\mathbf{U}_x, \mathbf{\Sigma}_x] = \text{eig}(\mathbf{R}_X) \quad (15)$$

where $\mathbf{\Sigma}_x$ is the real-valued eigenvalue diagonal matrix and \mathbf{U}_x is the orthogonal eigenmatrix. We obtain the number of targets k_s by performing 1D CA-CFAR detection on $\mathbf{\Sigma}_x$.

Construct $\mathbf{U}_N = \mathbf{U}_x(:, 1 : N_s - N_x)$ as the noise subspace basis. Then we can obtain the spatial angular spectrum function as [12]

$$f_a(\mathbf{p}; \mathbf{U}_N) = \mathbf{a}^H(\mathbf{p}) \mathbf{U}_N (\mathbf{U}_N)^H \mathbf{a}(\mathbf{p}) \quad (16)$$

where $\mathbf{p} = (\theta, \varphi)$ is the 2D angle, $\mathbf{a}(\mathbf{p})$ is given in (2). The spatial pseudo-spectrum is represented as [12]

$$S_a^{row}(\mathbf{p}; \mathbf{U}_N) = \left[\mathbf{a}^H(\mathbf{p}) \mathbf{U}_N (\mathbf{U}_N)^H \mathbf{a}(\mathbf{p}) \right]^{-1} \quad (17)$$

Similarly we can obtain $S_a^{col}(\mathbf{p}; \mathbf{U}_N)$ by taking the above operation for $(\mathbf{A}_{k_m})_{1,:}$. We obtained the estimated DoAs by performing 2D CA-CFAR detection on $S_a(\mathbf{p}; \mathbf{U}_N) = S_a^{col}(\mathbf{p}; \mathbf{U}_N) \odot S_a^{row}(\mathbf{p}; \mathbf{U}_N)$. \odot represents Hadamard product.

As shown in Fig. 7 (b), the noise of the 2D CA-CFAR is determined by averaging the N_R reference cells excluding the protection cell and the CUT.

$$\bar{\mu} = \frac{1}{N_R} \sum_{n=1}^{N_R} X_n \quad (18)$$

where X_n represents the reference unit value. The detection threshold of this CUT can be calculated from $T = T_f \times \bar{\mu}$ where T_f is given by (13), and the 2D adaptive detection threshold can be obtained by applying the above operations to all CUTs in $S_a(\mathbf{p}; \mathbf{U}_N)$ as shown in Fig. 7 (e)-(f).

The overall flow is shown in Algorithm. 1. Besides, we use the echoes of DL communication signals in the 5G mmWave band to realize the ISAC imaging without occupying additional communication resources. Therefore, the DL communication in our ISAC system is the same as the traditional communication system.

IV. NUMERICAL AND SIMULATION RESULTS

In this section, we firstly present our simulation parameters, then compare with traditional 4D-FFT imaging algorithm [4] to demonstrate the superiority of our proposed algorithm. Then the metrics we proposed for evaluating the imaging performance of ISAC is introduced. And the factors affecting the imaging performance are extensively studied.

Algorithm 1 ISAC Imaging Signal Processing

Input: ISAC Received Signal $y_{n,m}^{Rx}(t)$

Output: Reconstructed 4D scattering point cloud

- 1: Get the detection information matrix \mathbf{A}_S
- 2: Obtaining RDM using 2D-FFT algorithm
- 3: Obtaining RDM by detecting RDM with OSCA-CFAR
- 4: Constructing DoAs detection manifold \mathbf{A}_{k_m}
- 5: Decorrelation by using spatial smoothing algorithm
- 6: Get the MUSIC search pseudo-spectrum
- 7: Detecting DoAs with CA-CFAR
- 8: **end for**
- 9: Reduction of detection results to 4D point cloud
- 10: **return** ISAC imaging results

A. Simulation Parameter Setting

TABLE I
SIMULATION SYSTEM PARAMETERS

Parameter names	Value or Specification
MIMO size	2×2 -Tx/8 \times 8-Rx/16 \times 16-VRx
Carrier frequency	70GHz
Bandwidth	491.52MHz
Subcarrier spacing	240kHz
Subcarrier count	2048
OFDM symbol count	224
Slot count	16
Cyclic Prefix ratio	1/4
Cyclic Suffix ratio	1/32
PRS time slot interval	4
PRS structure	Comb4
Number of OFDM symbols occupied by PRS per slot	12
Number of spatially smoothed subarray elements	8

B. Qualitative Analysis of Imaging Results

As shown in Fig. 9, the imaging results obtained by the 4D-FFT algorithm and our proposed algorithm at SNR of -20 dB, -5 dB, and 10 dB are depicted for the qualitative analysis. Horizontal comparisons of Fig. 9 (a)-(c) and (d)-(f) show that the image point cloud density gradually improves with the increase of the SNR, and the imaging effect becomes better gradually; the vertical comparisons show that our proposed ISAC imaging signal processing method based on the 2D-FFT with 2D-MUSIC can obtain higher point cloud density and imaging quality compared with 4D-FFT.

C. Quantitative Analysis of Imaging Results

In order to solve the problem that ISAC 4D imaging quality is difficult to be measured quantitatively, we propose a multi-dimensional evaluation metric for 4D ISAC imaging as shown in Fig. 10. We measure image quality in terms of overall imaging deviation; the larger the deviation the worse the imaging quality, and vice versa. The overall 4D imaging deviation is divided into two parts: spatial and kinematic features. The

V. CONCLUSION

In this paper, we propose an ISAC 4D imaging system based on 2D-FFT with 2D-MUSIC using 5G DL mmWave signals. We introduce a two-stage CFAR detection algorithm, optimize the DoA estimation and velocity-range estimation processes, and design a transceiver antenna arrangement based on the MIMO virtual aperture technique. Besides, we propose a new evaluation metric for ISAC 4D imaging quality. The simulation results show that our proposed method can obtain ISAC 4D imaging results with higher 4D point cloud density and higher imaging accuracy compared to the traditional methods.

In the future, we will build ISAC 4D imaging datasets and introduce deep learning models to realize more complex functions.

REFERENCES

- [1] L. Wang, Z. Wei, L. Su, Z. Feng, H. Wu, and D. Xue, "Coherent compensation based isac signal processing for long-range sensing," 2023.
- [2] S. Sun, A. P. Petropulu, and H. V. Poor, "Mimo radar for advanced driver-assistance systems and autonomous driving: Advantages and challenges," *IEEE Signal Processing Magazine*, vol. 37, no. 4, pp. 98–117, 2020.
- [3] M. Jiang, G. Xu, H. Pei, Z. Feng, S. Ma, H. Zhang, and W. Hong, "4d high-resolution imagery of point clouds for automotive mmwave radar," *IEEE Transactions on Intelligent Transportation Systems*, 2023.
- [4] A. Santra, A. R. Ganis, J. Mietzner, and V. Ziegler, "Ambiguity function and imaging performance of coded fmcw waveforms with fast 4d receiver processing in mimo radar," *Digital Signal Processing*, vol. 97, p. 102618, 2020.
- [5] S. Sun and Y. D. Zhang, "4d automotive radar sensing for autonomous vehicles: A sparsity-oriented approach," *IEEE Journal of Selected Topics in Signal Processing*, vol. 15, no. 4, pp. 879–891, 2021.
- [6] X. Chen, Z. Feng, Z. Wei, X. Yuan, P. Zhang, J. A. Zhang, and H. Yang, "Multiple signal classification based joint communication and sensing system," *IEEE Transactions on Wireless Communications*, 2023.
- [7] J. Guan, A. Paidimarri, A. Valdes-Garcia, and B. Sadhu, "3-d imaging using millimeter-wave 5g signal reflections," *IEEE Transactions on Microwave Theory and Techniques*, vol. 69, no. 6, pp. 2936–2948, 2021.
- [8] M. Stolz, M. Wolf, F. Meinel, M. Kunert, and W. Menzel, "A new antenna array and signal processing concept for an automotive 4d radar," in *2018 15th European Radar Conference (EuRAD)*. IEEE, 2018, pp. 63–66.
- [9] X. Gao, G. Xing, S. Roy, and H. Liu, "Experiments with mmwave automotive radar test-bed," in *2019 53rd asilomar conference on signals, systems, and computers*. IEEE, 2019, pp. 1–6.
- [10] Z. Wei, Y. Wang, L. Ma, S. Yang, Z. Feng, C. Pan, Q. Zhang, Y. Wang, H. Wu, and P. Zhang, "5g prs-based sensing: A sensing reference signal approach for joint sensing and communication system," *IEEE Transactions on Vehicular Technology*, vol. 72, no. 3, pp. 3250–3263, 2022.
- [11] C. Sturm and W. Wiesbeck, "Waveform design and signal processing aspects for fusion of wireless communications and radar sensing," *Proceedings of the IEEE*, vol. 99, no. 7, pp. 1236–1259, 2011.
- [12] M. Haardt, M. Pesavento, F. Roemer, and M. N. El Korso, "Subspace methods and exploitation of special array structures," in *Academic Press Library in Signal Processing*. Elsevier, 2014, vol. 3, pp. 651–717.
- [13] D. P. Huttenlocher, G. A. Klanderman, and W. J. Rucklidge, "Comparing images using the hausdorff distance," *IEEE Transactions on pattern analysis and machine intelligence*, vol. 15, no. 9, pp. 850–863, 1993.

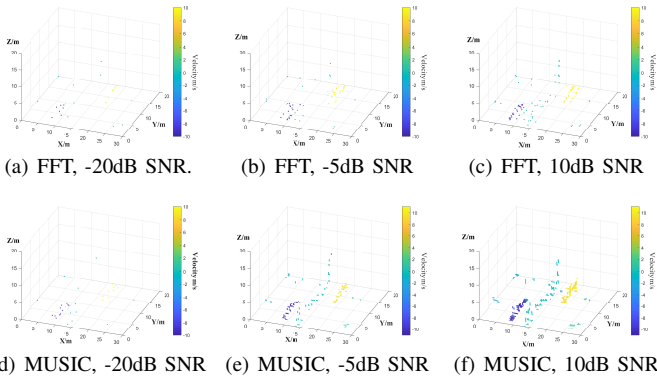


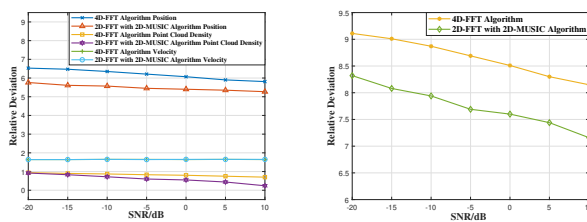
Fig. 9. (a)-(c) are the ISAC imaging results under different SNR based on the 4D-FFT algorithm, and (d)-(f) are the ISAC imaging results under different SNR based on the 2D-FFT with 2D-MUSIC algorithm.

spatial deviation is determined by the coordinate difference and the point cloud density difference between the imaging result and the original scene, where we measure the coordinate difference by calculating the Hausdorff distance [13] using each of the three 2D projections of the 3D coordinates. The kinematic deviation is measured by Normalized Mean Square Error (NMSE) between the velocity of the main scattering points of the imaging result and the original scene.



Fig. 10. Components of ISAC Imaging Deviation.

The trends of the components of the ISAC 4D imaging deviation with SNR are shown in Fig. 11 (a), and the overall trend is shown in Fig. 11 (b). It is worth mentioning that since our proposed algorithm depends on the 2D-FFT algorithm for the estimation of velocity and distance, the trend of kinematic deviation is the same for both algorithms. The results show that the ISAC 4D imaging quality improves with the SNR, and the imaging quality of our proposed algorithm is significantly higher than that of the FFT-based method.



(a) Comparison of various components of 4D ISAC imaging deviation for the two algorithms. (b) Overall Imaging Deviation Comparison.

Fig. 11. Variation curve of ISAC imaging deviation with SNR.